JOURNAL OF GEOPHYSICAL RESEARCH, VOL. 115, A07209, doi:10.1029/2009JA015075, 2010

Global simulation of EMIC wave excitation during the 21 April 2001 storm from coupled RCM-RAM-HOTRAY modeling

Lunjin Chen,[1] Richard M. Thorne,[1] Vania K. Jordanova,[2] Chih-Ping Wang,[1] Matina Gkioulidou,[1] Larry Lyons,[1] and Richard B. Horne[3]

Received 6 November 2009; revised 10 February 2010; accepted 18 February 2010; published 15 July 2010.

[1] The global distribution and spectral properties of electromagnetic ion cyclotron (EMIC) waves in the He^+ band are simulated for the 21 April 2001 storm using a combination of three different codes: the Rice Convection Model, the Ring current-Atmospheric interactions Model, and the HOTRAY ray tracing code (incorporated with growth rate solver). During the storm main phase, injected ions exhibit a non-Maxwellian distribution with pronounced phase space density minima at energies around a few keV. Ring current H^+ injected from the plasma sheet provides the source of free energy for EMIC excitation during the storm. Significant wave gain is confined to a limited spatial region inside the storm time plume and maximizes at the eastward edge of the plume in the dusk and premidnight sector. The excited waves are also able to resonate and scatter relativistic electrons, but the minimum electron resonant energy is generally above 3 MeV.

Citation: Chen, L., R. M. Thorne, V. K. Jordanova, C.-P. Wang, M. Gkioulidou, L. Lyons, and R. B. Horne (2010), Global simulation of EMIC wave excitation during the 21 April 2001 storm from coupled RCM-RAM-HOTRAY modeling, *J. Geophys. Res.*, *115*, A07209, doi:10.1029/2009JA015075.

1. Introduction

[2] Electromagnetic ion cyclotron (EMIC) waves can be excited by an anisotropic distribution of energetic ring current ions, with energies near a few tens of keV. Previous studies [e.g, *Gomberoff and Neira*, 1983, *Young et al.*, 1981; *Horne and Thorne*, 1993, *Jordanova et al.*, 1997] have shown that the generation and propagation characteristics of EMIC waves in a multi-ion (H^+; He^+; O^+) plasma are profoundly controlled by ion fractional composition and by the ratio of electron plasma to gyro frequency $\omega_{pe}/|\Omega e|$. EMIC waves can also be guided by density gradients at the plasmapause, which keep the wave normal angle small and significantly enhance the path integrated gain [*Thorne and Horne*, 1997]. Previous observational studies have shown that EMIC waves are enhanced during magnetic storms [*Bräysy et al.*, 1998, *Erlandson and Ukhorskiy*, 2001 with the most intense emissions confined to the dusk sector [*Meredith et al.*, 2003], consistent with the drift path of injected ring current ions into the storm time plasmapause and plume [*Cornwall and Schulz*, 1971, *Jordanova et al.*, 2006] and the excitation of detached subauroral proton arcs [*Spasojević et al.*, 2004, *Jordanova et al.*, 2007]. The present paper describes the first attempt to model the global excitation and spectral properties of inner magnetospheric EMIC waves during storm conditions under a new grant from the NASA Heliophysics Theory program, using a combination of three well established models described below.

[3] EMIC waves excited during storms can also resonate with relativistic electrons, causing rapid scattering loss [*Thorne and Kennel*, 1971, *Lyons and Thorne*, 1973, *Jordanova et al.*, 2008], but the minimum energy for electron resonance is strongly dependent on ion composition and plasma density [*Summers and Thorne*, 2003, *Albert*, 2003, *Li et al.*, 2007]. Specifically, the electron resonant energy is significantly reduced for EMIC waves just below the He^+ ion gyrofrequency, which can be excited by an anisotropic distribution of ring current H^+ [*Kozyra et al.*, 1984, *Horne and Thorne*, 1993] with energies near a few keV [*Meredith et al.*, 2003]. It has been shown that the wave gain just below the He^+ gyrofrequency is much greater than that just below the O^+ and H^+ gyrofrequency [*Horne and Thorne*, 1993, 1994]. A statistical study of EMIC waves observed on CRRES [*Meredith et al.*, 2003] showed that the minimum resonant energy for electrons was generally $\geq$ 2 MeV for the majority of EMIC wave events, but about 11% of reported EMIC events had minimum resonant energy <2 MeV. These observed EMIC waves interacting with such low-energy electrons were in the He^+ band with wave frequency very close to He^+ gyrofrequency. EMIC waves with amplitude up to 10 nT have been observed during the main phase of magnetic storms [*Erlandson and Ukhorskiy*, 2001], capable of inducing rapid scattering of relativistic electrons at a rate comparable to the strong diffusion limit [*Shprits et al.*, 2009]. Such relativistic electron loss is confined to high-density regions just inside

[1]Department of Atmospheric Sciences, University of California, Los Angeles, California, USA.
[2]Los Alamos National Laboratory, Los Alamos, New Mexico, USA.
[3]British Antarctic Survey, Natural Environment Research Council, Cambridge, UK.

0148-0227/10/2009JA015075

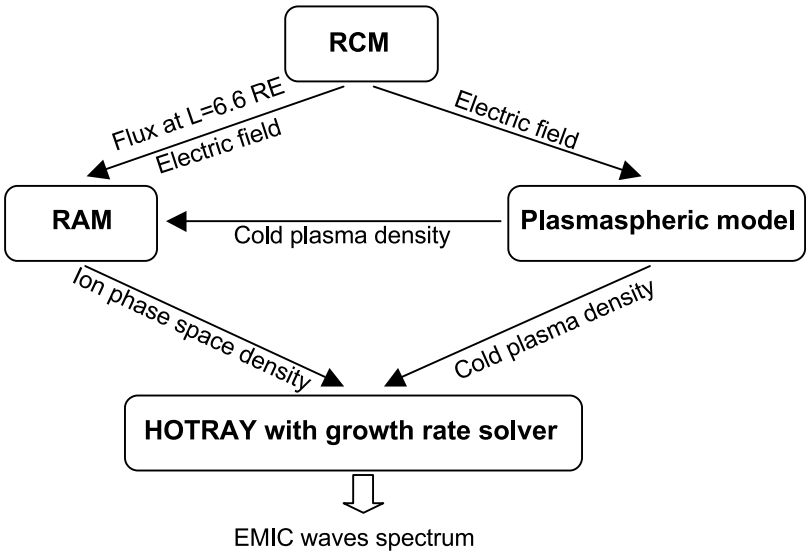

Figure 1. Flowchart of EMIC wave spectrum simulation combining RCM, RAM, and HOTRAY codes.

the plasmapause or within dayside drainage plumes [*Thorne et al.*, 2006, *Jordanova et al.*, 2008]. Electron density inside such storm time plumes exhibits fine-scale structures [*Goldstein et al.*, 2004, *Spasojević et al.*, 2003, 2004]. Recently, *Chen et al.* [2009] has shown this density structure can enhance the wave excitation, especially at frequencies close to the He^+ gyrofrequency, and thus reduce the electron minimum resonant energy to below 2 MeV.

[4] Instability of EMIC waves has been studied for plasmas with various types of proton distributions, e.g., bi-Maxwellian distribution [*Horne and Thorne*, 1993, 1994, *Chen et al.*, 2009] and kappa distribution [*Summers and Thorne*, 1991; *Xiao et al.*, 2007]. Due to inhomogeneity of the magnetosphere (e.g., spatial variation of thermal plasma density and the Earth's magnetic field), propagation characteristics must be carefully taken into account when one considers the excitation of EMIC waves in this environment. The HOTRAY code was initially designed to calculate the path-integrated gain of plasma waves in a fully hot plasma where each species is modeled by a combination of one or more bi-Maxwellian components. However, during storm conditions, the injected hot proton distribution can be far from Maxwellian. Consequently, in this initial study of EMIC wave excitation on the global scale, we introduce a new technique to evaluate the path integrated wave gain (Figure 1). The Ring current-Atmosphere interactions Model (RAM) is used to simulate the evolution of ring current ions phase space density (PSD) and plasmaspheric density during the 21 April 2001 storm, driven by the convection electric field and flux boundary conditions provided by the Rice Convection Model (RCM) code. Ray tracing with HOTRAY, together with the formulation of *Kennel* [1966] to evaluate local convective growth rate, using the ion distribution functions obtained from RAM, is used to simulate the global distribution of EMIC wave gain.

[5] The outline of this paper is as follows. In section 2, the ring current and thermal plasma density model obtained from the combined RAM and RCM simulation is described. A ray tracing technique is used in section 3 to study the propagation characteristics of EMIC waves in the He^+ band, and the path-integrated gain is also evaluated for the ring current proton distribution obtained from the RAM simulation. The results for the global distribution of EMIC wave excitation and their spectral properties are presented and their ability to scatter MeV electrons is evaluated in section 4. Finally, we summarize our principal conclusions and discuss the relevance of our findings to future modeling of global ring current and radiation belt dynamics.

2. Ring Current Modeling

[6] A NASA Heliophysics Theory project was initiated at UCLA in 2008, aimed at developing a global model for the origin of two dominant magnetospheric plasma waves (Chorus and EMIC waves), which affect the dynamical behavior of ring current and radiation belt particles. This objective can be achieved by combining three codes (see flowchart in Figure 1): RCM [*Toffoletto et al.*, 2003, and references therein], RAM [*Jordanova et al.*, 1996, 1997, and references therein] and the HOTRAY code [*Horne*, 1989]. The RCM is an established physical model of the middle magnetosphere and plasma sheet that includes coupling to the ionosphere, by using a multifluid formalism to describe adiabatically drifting isotropic particle distributions in a self-consistently computed electric field and a specified magnetic field. The Tsyganenko 96 (T96) magnetic field model [*Tsyganenko*, 1995, 1996] is used for this study. The RCM is used to treat the transport of ions and electrons into the inner magnetosphere from the distant plasma sheet, modeling the proton and electron energy spectra with isotropic particle velocity space distributions for both species. The RCM's outer boundary is set at $\approx 20\ R_E$, the proton and electron energy spectra at the boundary is established as a function of MLT and the interplanetary conditions, based on analysis of 11 years (1995–2005) of the Geotail LEP electron and ion fluxes from ≈0.04 to 40 keV data and the Geotail EPIC ion data (46 to 3000 keV) and assuming all ions are protons [*Wang et al.*, 2007, *Gkioulidou et al.*, 2009]. The time-dependent cross polar-cap potential drop ($\Delta\Phi_{PCP}$) and the Z component of interplanetary magnetic

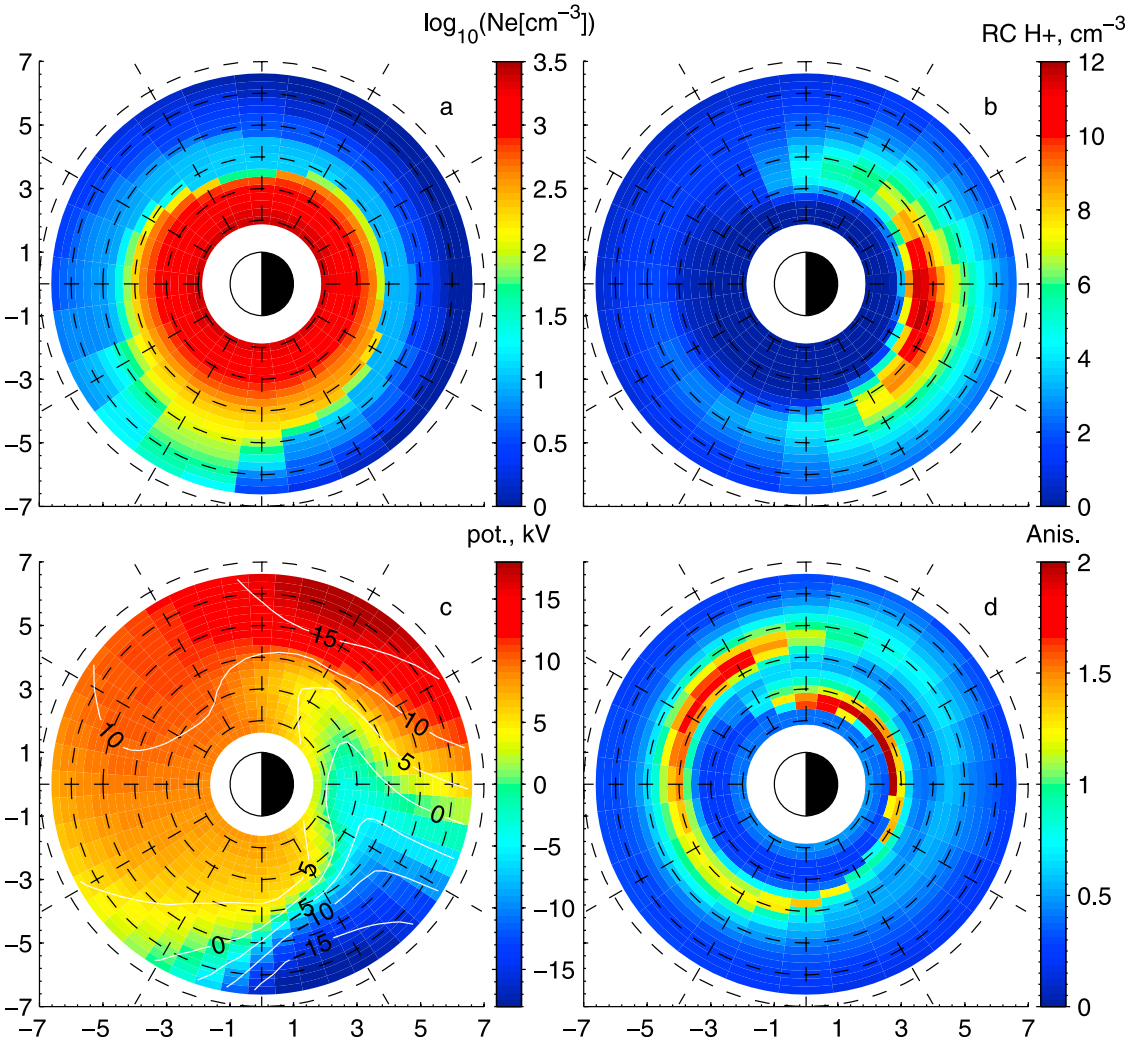

Figure 2. RCM and RAM simulation of the 21 April 2001 storm during the main phase, $t = 40$ h. (a) The equatorial thermal plasma density, (b) equatorial ring current H^+ density, (c) electric potential contours from RCM simulation, and (d) anisotropy of ring current H^+ ($T_\perp/T_\parallel - 1$). Concentric dashed circles are spaced 1 R_E apart, and MLT spokes are drawn every 2 hours.

field (IMF B_z) are used as inputs for both the outer particle boundary condition and for the T96 model. To establish the initial condition for the RCM, we first ran the simulation under a time-independent $\Delta\ \Phi_{PCP}$ of 30 kV with quiet time T96 fields (IMF $B_z = 0$ nT) until it reached a steady state. This steady state is used as the initial condition. The electric field distribution in the inner magnetosphere modeled by the RCM is maintained self-consistently with the plasma pressure by taking into account the effect of the ionosphere through the field-aligned current and thus the effect of the penetrating and shielding electric fields [*Toffoletto et al.*, 2003].

[7] The energy spectrum modeled by the RCM at geosynchronous orbit (≈6.6 R_E) is used to derive the energetic particle distribution function at the outer boundary condition (or source population) for the RAM simulation. Since the RCM assumes isotropic particle distributions for both electrons and protons, the ion composition and pitch angle anisotropy of ring current ions at this outer boundary is inferred from empirical studies as a function of solar and geomagnetic activity [*Young et al.*, 1982, *Roeder et al.*, 2005]. Subsequently, the RAM code solves fundamental kinetic equations to simulate the evolution of the distribution function of ring current electrons and ions, including H^+, He^+ and O^+ with energy from 500 eV to 400 keV, in the inner magnetosphere $2.0 \le L \le 6.5$. The RAM simulation takes into account various loss and transport processes including charge exchange, Coulomb collisions, atmospheric loss, escape from magnetopause, convective transport, gradient drifting and radial diffusion. The RAM code is coupled with a plasmaspheric model [*Rasmussen et al.*, 1993] that was developed further to use an arbitrary electric field by *Jordanova et al.* [2006]. Therefore, the electric field output from the RCM is used to drive both the plasmaspheric density model and the convective transport of ring current ions.

[8] The RAM code was used to simulate ring current species evolution during the 21 April 2001 storm for a 72 h period with $t = 0$ h defined as 00UT on 21 April. Two intervals, $t = 40$ (Dst min) and $t = 48$ h (recovery phase), have been selected to evaluate the global distribution of EMIC waves in this study. The equatorial plasmaspheric electron

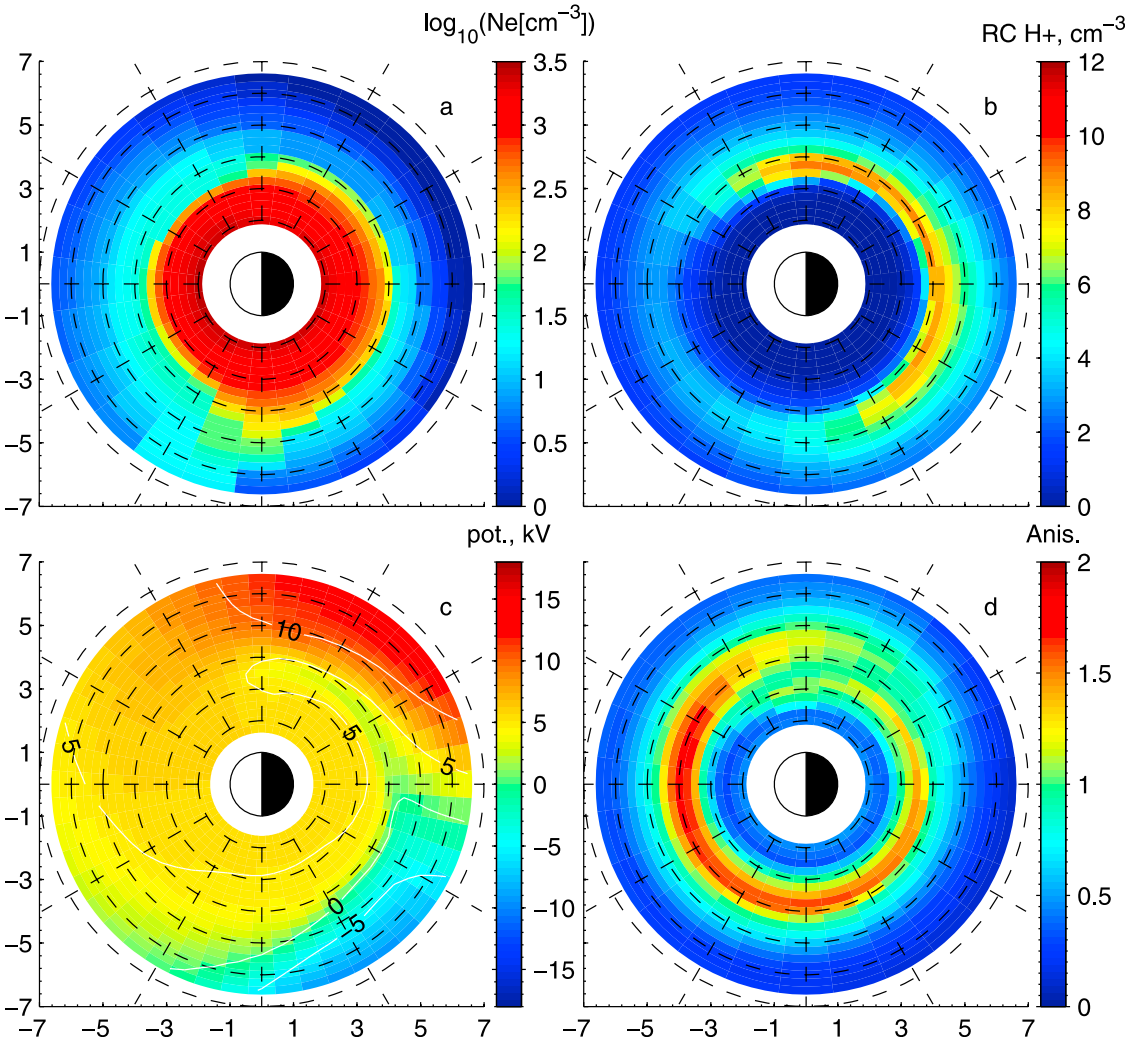

Figure 3. The same format as Figure 2 during the storm recovery, t = 48 h.

density, ring current H^+ density, ring current H^+ temperature anisotropy and equatorial electric potential are shown in Figure 2 (t = 40 h) and Figure 3 (t = 48 h). The temperature anisotropy here is defined as $T_\perp/T_\parallel - 1$, where $T_\perp$ and $T_\parallel$ are the temperature perpendicular and parallel to the ambient magnetic field. At t = 40 h, a high-density plume has formed on the duskside. Ring current ions are injected from the plasma sheet, forming a partial ring current in the night sector, $3 < L < 5$. Electric potential from the RCM simulation shows shielding on the nightside at $L < 3$ and convergence of electric field in the postmidnight sector, which results in field-aligned current and thus ionosphere-magnetosphere interaction. Large ring current H^+ anisotropy (>1) develops at lower L shells (<3) on the nightside mostly due to rapid charge exchange loss [*Jordanova et al.*, 1996], and at $3.5 < L < 5.5$ on the dayside due to collisional losses and energy-dependent drifting [*Jordanova et al.*, 1999]. The total ring current H^+ number density maximizes at $3.5 < L < 4.5$ on the nightside where the anisotropy is quite low (<0.5), and then decreases away from the nightside. During the storm recovery phase (Figure 3), the plume narrows and rotates eastward. The convergence of electric field extends to the dawnside, leading to an increase in ring current ion density on the dawnside, especially for low-energy ions. The partial ring current becomes more symmetric. Ring current proton anisotropy is further enhanced on the nightside and duskside, and the ring current proton number density increases on the dayside and duskside.

[9] The H^+ PSD during the main phase (t = 40 h) and recovery phase (t = 48 h) at the locations L = 4.5 at midnight (MLT = 00), dusk (MLT = 18) and noon (MLT = 12) are shown in Figure 4. The PSD at midnight (Figures 4a and 4b) is essentially bi-Maxwellian with a loss cone feature of a few degrees and $T_\perp > T_\parallel$, as a result of injection on the nightside. The PSD in the dusk sector (Figures 4c and 4d), however, shows a ring-type distribution with a pronounced peak along the $v_\perp$ axis at about $T_\perp$ = 11 keV at t = 40 h and 7 keV at t = 48 h (5.2 keV in energy is equivalent to 10^6 ms^{-1} in velocity for H^+ species.). This feature develops over the MLT range between prenoon and the duskside as a result of energy-dependent particle injection. Ring current ions of intermediate energy (≈ a few keV) have little access to this location; ions above 10 keV follow drift paths dominated by westward gradient drift, while ions below 1 keV are predominately subject to electric field drift in the eastward direction [*Jordanova1 et al.*, 1999 and references therein]. As a consequence of the energy-dependent injection, a pro-

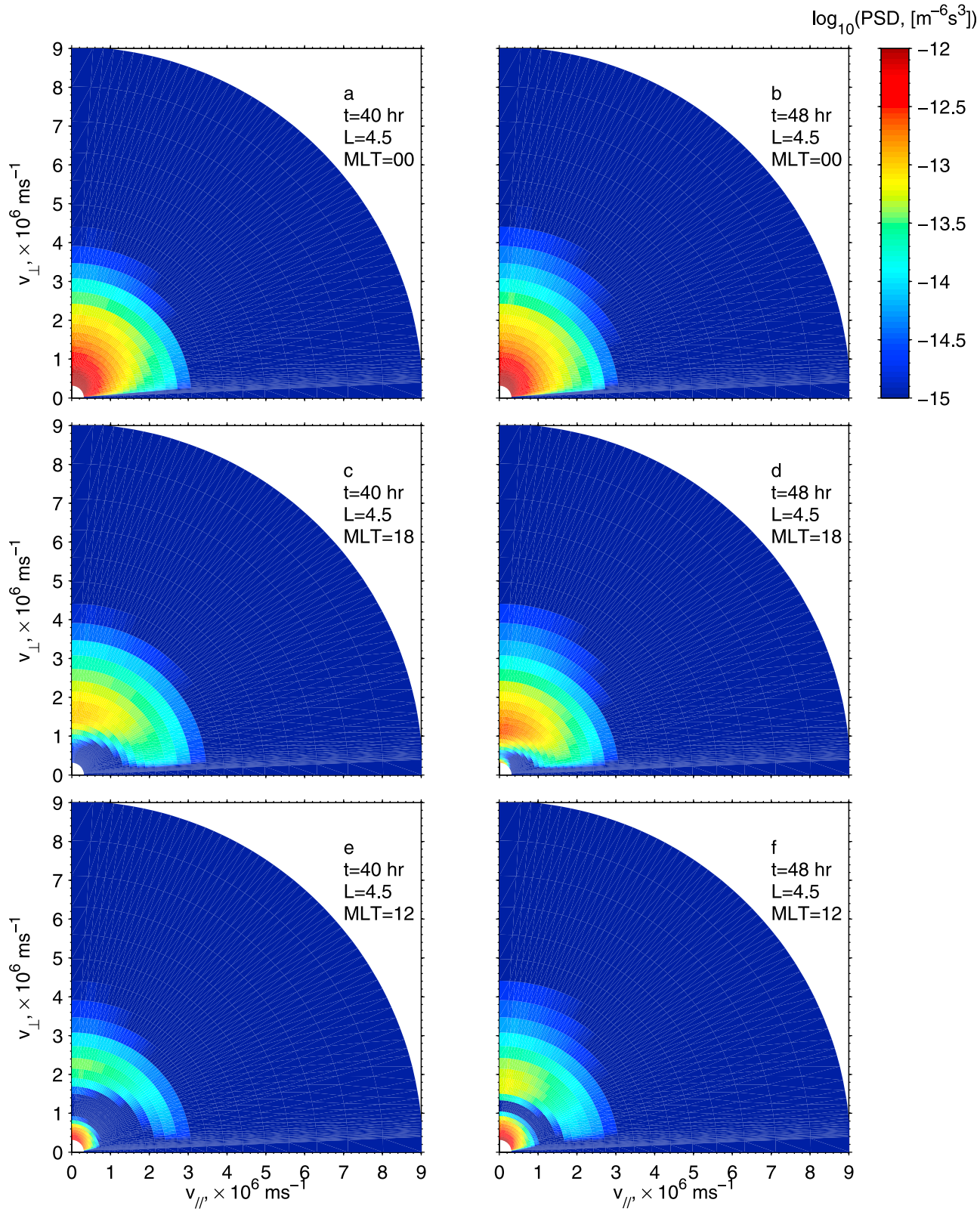

Figure 4. Examples of phase space density of ring current protons simulated by the RAM code: at L = 4.5 during the storm main phase (t = 40 h) and recovery (t = 48 h) at three different MLT, showing the evolution of ion ring distribution at dusk and on the dayside.

nounced separate low-energy component (energy less than a few keV) develops on the dayside. This isolated feature also extends to the duskside during the recovery phase (Figure 4d) but not during the main phase (Figure 4c), because of the time delay (≈ of hours) for these low-energy particles to be transported from midnight to the duskside (eastwardly) due to slow electric field drift motion. At noon (Figures 4e and 4f), the ring-type phase space density becomes smaller and the lower-energy component becomes stronger than on the duskside. The positive derivatives of the PSD f with respect to $v_\perp$ and $v_\parallel$ just below the ring energy (the energy where f peaks), $\frac{\partial f}{\partial v_\perp} > 0$ and $\frac{\partial f}{\partial v_\parallel} > 0$, suggest that the particle distribution is unstable. The anisotropic distribution of H^+ with $\frac{\partial f}{\partial \alpha} > 0$, e.g., PSD on the nightside, also provides the source of free energy for L mode field-aligned EMIC waves in the frequency band $\omega < \frac{A^+}{A^++1}\Omega_{H^+}$ [*Kennel and Petschek*, 1966], where α is pitch angle, A^+ is anisotropy for H^+ species defined as a function of resonant velocity V_R [*Kennel and Petschek*, 1966]:

$$A^+(V_R) = \left.\frac{\int_0^\infty v_\perp dv_\perp (v_\parallel \frac{\partial f}{\partial v_\perp} - v_\perp \frac{\partial f}{\partial v_\parallel})\frac{v_\perp}{v_\parallel}}{2\int_0^\infty v_\perp dv_\perp f}\right|_{v_\parallel = V_R} \quad (1)$$

[10] A positive value of $T_\perp/T_\parallel - 1$ is an indicator of potential EMIC wave instability, but cannot itself yield the frequency range where EMIC waves can grow. For parallel propagation, EMIC wave growth rate is dependent on the fractional number of resonant protons and the ion anisotropy (A^+) at resonant energies [*Kennel and Petschek*, 1966], which are determined by wave frequency and the thermal plasma environment. Waves with frequency closer to the He^+ gyrofrequency Ω_{He^+} in the higher-density thermal plasma region (e.g., inside the plume), can resonate with ring current protons at lower energy (~1−10 keV).

3. Ray Tracing Model

[11] The PSD of ring current energetic ions and the plasmaspheric electron density obtained from the RAM simulation are used to evaluate the path integrated gain of EMIC waves in the He^+ band between Ω_{O^+} and Ω_{He^+} (Figure 1). The evaluation is preformed by the following three steps.

[12] First, ray tracing is performed in order to obtain the propagation characteristics of the EMIC waves in the multi-ion (H^+–He^+–O^+) magnetosphere. We use the HOTRAY code [*Horne*, 1989] which has been extensively applied to electromagnetic and electrostatic waves, including EMIC waves in the Earth's magnetosphere [e.g., *Horne and Thorne*, 1993, 1994]. The code can trace any type of wave in a hot magnetized plasma with weak growth or damping, provided the wave remains linear. The ray tracing method assumes that gradients in the medium, notably the plasma density and magnetic field gradients, are small compared to the wavelength, and that the gradients remain continuous. The HOTRAY code checks this condition at every step along the raypath. The ray tracing equations [*Horne*, 1989, equations (1) and (2)] are integrated with respect to time to find the new position, and wave number at each time step. Although HOTRAY can also solve the hot plasma dispersion relation to yield a complex wave vector **k**, whose imaginary part may be used to calculate the path integrated gain, such analysis is limited to the cases where the distribution function of each component follows the Ashour-Abdalla and Kennel distribution [*Ashour-Abdalla and Kennel*, 1978]. Although the PSD from the RAM can be fit by such bi-Maxwellian type distributions in the sector near midnight (Figures 4a and 4b), the simulated ring current proton near the duskside cannot be fit by such a distribution, because it consists of a higher-energy component and a separate lower-energy component, between which no significant PSD is present. Therefore, instead of using HOTRAY to calculate the growth rate, we introduce a new method to calculate the local growth rate (second step), which can be applied for any type of distribution function.

[13] For the purpose of ray tracing, a dipole magnetic field is assumed and a smooth density model is constructed from the equatorial density simulation (the Rasmussen model) by the RAM code. The density simulation has grids of every 0.25 in L and every half hour in MLT. This discrete density model at each MLT is interpolated to obtain a smooth radial plasmaspheric electron density distribution in the meridian plane through cubic spline interpolation. Constant density along the magnetic field lines is assumed, which is not a critical assumption since the source of EMIC wave excitation is confined to within about 10° latitude of the equator and the subsequent propagation and reflection at high latitude [e.g., *Thorne and Horne*, 1992, 1994, *Horne and Thorne*, 1997] are not treated in this paper. Since the fractional thermal ion composition greatly affects propagation characteristics of EMIC waves and is not explicitly simulated in the Rasmussen model, a typical storm time thermal ion composition, η_{H^+} = 77%, η_{He^+} = 20%, η_{O^+} = 3%, is assumed, following *Jordanova et al.* [2008]. The temperature of thermal electrons is set to 10 eV and that of all ions is set to 1 eV [*Chen et al.*, 2009].

[14] For simplicity, we only perform two-dimensional ray tracing in the meridian plane at various MLT, ignoring the azimuthal propagation, which is justified by the almost field aligned wave group velocity of EMIC waves in the He^+ band over the frequency range, $\omega_{cr} < \omega < \Omega_{He^+}$ [e.g., *Horne and Thorne*, 1993], where ω_{cr} is the crossover frequency between the O^+ and He^+ gyrofrequencies and Ω_{He^+} is the He^+ gyrofrequency.

[15] Secondly, the ring current ion PSD obtained from the RAM simulations is used to evaluate the growth rate of EMIC waves at each location along the raypath, following a corrected version of equation (3.9) in the work of *Kennel* [1966]:

$$\begin{aligned}\gamma_s = {} & 2\pi^2 \frac{\omega_{ps}^2}{\omega|k_\parallel|\frac{\partial D^{(0)}}{\partial \omega}} \int_0^\infty v_\perp dv_\perp \int_{-\infty}^{+\infty} dv_\parallel \sum_m \delta(v_\parallel - \frac{\omega - m\Omega_s}{k_\parallel}) \\ & \cdot \Big[G_{1s}\Big((P - n^2\sin^2\theta)\big[2(L-n^2)v_\perp J_{m+1}^2 + 2v_\perp(R-n^2)J_{m-1}^2 \\ & + n^2\sin^2\theta v_\perp (J_{m+1} - J_{m-1})^2\big] \\ & - n^2\cos\theta\sin\theta\big[2v_\parallel J_m(J_{m+1}(R-n^2) + J_{m-1}(L-n^2)) \\ & + n^2\cos\theta\sin\theta v_\perp (J_{m+1} - J_{m-1})^2\big]\Big) \\ & + G_{2s}\Big(4v_\parallel J_m\big[(L-n^2)(R-n^2) + n^2\sin^2\theta(S-n^2)\big] \\ & - 2n^2\cos\theta\sin\theta\big[(R-n^2)v_\perp J_{m-1} + (L-n^2)v_\perp J_{m+1}\big]\Big)\Big] \quad (2)\end{aligned}$$

where the subscript s denotes hot species (ring current H^+, He^+ or O^+ in our case) and the subscript m harmonic resonance, γ_s is temporal growth rate due to the contribution of hot species s, $D^{(0)}$ is the determinant of cold plasma dispersion relation matrix defined in equation (3.5) of *Kennel* [1966], R, L, P and S are Stix coefficients, based on the cold component of plasma, θ, ω and n are wave normal angle, frequency and wave refractive index, respectively, J_m are Bessel functions of order m with argument $\frac{k_\perp v_\perp}{\Omega_s}$, $\Omega_s = q_s B/m_s$. G_{1s} and G_{2s} involves gradients in the PSD, defined as,

$$G_{1s} = \frac{\partial F_s}{\partial v_\perp} - \frac{k_\parallel}{\omega}\left(v_\parallel \frac{\partial F_s}{\partial v_\perp} - v_\perp \frac{\partial F_s}{\partial v_\parallel}\right) \tag{3}$$

and

$$G_{2s} = J_m\left[\frac{\partial F_s}{\partial v_\parallel} + \frac{m\Omega_s}{\omega v_\perp}\left(v_\parallel \frac{\partial F_s}{\partial v_\perp} - v_\perp \frac{\partial F_s}{\partial v_\parallel}\right)\right], \tag{4}$$

where F_s is the normalized distribution function of species s. It should be noted that there is a typo in the original paper, i.e., R and L in the fifth line of equation (3.9) of *Kennel* [1966] should be L and R, respectively. This formulation is strictly valid only when the temporal growth is much smaller than the wave frequency, $\gamma \ll \omega$, which can readily be checked. In the regime of small growth rate, the total growth is the sum of the temporal growth rate over all resonant species. The range of resonance harmonics m is set from −10 to 10 in our calculation.

[16] Thirdly, path-integrated gain is calculated by integrating the local growth rate along raypath:

$$\text{Gain, dB} = 20\ \log_{10}(\exp(\int \gamma dt)). \tag{5}$$

[17] Figure 5 shows examples of the propagation characteristics and net gain of the waves launched at t = 48 h, L = 4.5 and MLT = 19 with parallel propagation vector at the equator along the eastward edge of the plume, where a steep negative density gradient exists in the radial direction. As a result of the competition of wave refraction due to magnetic gradients and the negative density gradient, the wave vector is confined to small angles with respect to the ambient magnetic field, which enhances the net wave gain. Waves near 3.05 Ω_{O^+} launched at this location can obtain wave gain up to 50 dB along the raypath on one side of the equator, due to wave guidance and resonance with a large portion of H^+ ions of large and positive A^+. Waves with frequency ~3.65 Ω_{O^+} (closer to the He^+ gyrofrequency) can resonate with a larger portion of H^+ ions with lower $v_\parallel$, but the wave normal angle rapidly becomes oblique (≥60°). During the oblique propagation, wave growth stops and the net wave gain is only 2 dB. The wave normal angle of low-frequency (2.25 Ω_{O^+}) waves also remains small within 10 degrees in latitude. However, such waves do not resonate with a significant portion of particles ($E_\parallel$res > 25 keV), thus only obtaining wave gain of about 20 dB. Both electron and proton cyclotron resonant energies minimize at the equator for excited waves with the largest normalized wave frequency and zero wave normal angle. For most of the depicted waves, strong growth occurs in the region within a few degrees of the equator.

4. Global Distribution of Wave Gain

[18] The ray tracing illustrated in Figure 5 has been repeated multiple times, in each case varying one of initial parameters to obtain the global distribution of wave gain. Calculations are performed in step of 0.25 L for 3.75 < L < 5.5, every hour in MLT, every 0.1 in ω/Ω_{O^+} for $\omega_{cr} < \omega < 3\ \Omega_{O^+}$ and every 0.05 for 3 Ω_{O^+} < ω < 3.9 Ω_{O^+}, for conditions during the main phase (t = 40 h) and recovery phase (t = 48 h) of the storm. The maximum integrated wave gain is evaluated along each raypath as a function of initial parameters, i.e., L, MLT, ω/Ω_{O^+}, and t.

[19] As noted earlier, EMIC waves in this frequency range basically propagate along the field line, which allows us to associate the maximum path-integrated gain with the wave launching location. The wave gain obtained in such way is only one half of the net EMIC gain in the system, since we have only considered propagation on one side of the equator. The waves should obtain identical wave gain at the equator with zero wave normal angle if waves are traced backward along the half raypath from the location of maximum wave gain toward the equator [e.g., *Chen et al.*, 2009]. Consequently, the maximum wave gain would double if waves were launched from one side of the equator and propagate toward the other side. The full EMIC wave gain is shown in Figure 6 (t = 40 h) and Figure 7 (t = 48 h) as a function of normalized wave frequency ω/Ω_{O^+} (y axis) and MLT (x axis) for different L shell, represented by each row. The quantity $\log_{10}(N_e)$ as a function of MLT at different L, where N_e is in unit of cm^{-3}, is superimposed in white lines. At t = 40 h, the preferential location for EMIC wave excitation is on duskside 4 < L < 5, including the region at the eastward edge of the plume and the region inside the plume. This is in agreement with previous storm simulations with the RAM [e.g., *Jordanova et al.*, 2001, 2007]. Waves inside the plume experience gain above 30 dB in the frequency range centered at about ω = 3 Ω_{O^+}. However, the strongest wave gain (>60 dB) occurs at the eastward edge of the plume at slightly higher normalized frequencies. Because of high thermal electron density in those two regions, EMIC waves can resonate with a larger portion of ring current protons. Wave refraction due to density gradient on the edge of the plume counteracts against refraction due to magnetic field gradient (which tends to pull the wave vector away from the Earth), and thus waves are confined to small wave normal angles for a significant portion of raypath, enhancing the wave gain.

[20] On the westward edge of the plume, the wave gain is smaller than on the eastward edge for the following two reasons. First, the density gradient on the west edge is not as steep as on the east edge, because of the smoothing effect of plasmaspheric refilling on the dayside, which is simulated in the plasmaspheric model. Consequently, wave guidance on the western edge is not as effective as on the eastern side. Secondly, the number of energetic protons (~10 to 100 keV) resonating with EMIC waves is larger on the eastward side. Those energetic protons injected from the nightside follow westward magnetic gradient and curvature drift. During the westward drifting, ions are subject to gradual loss predom-

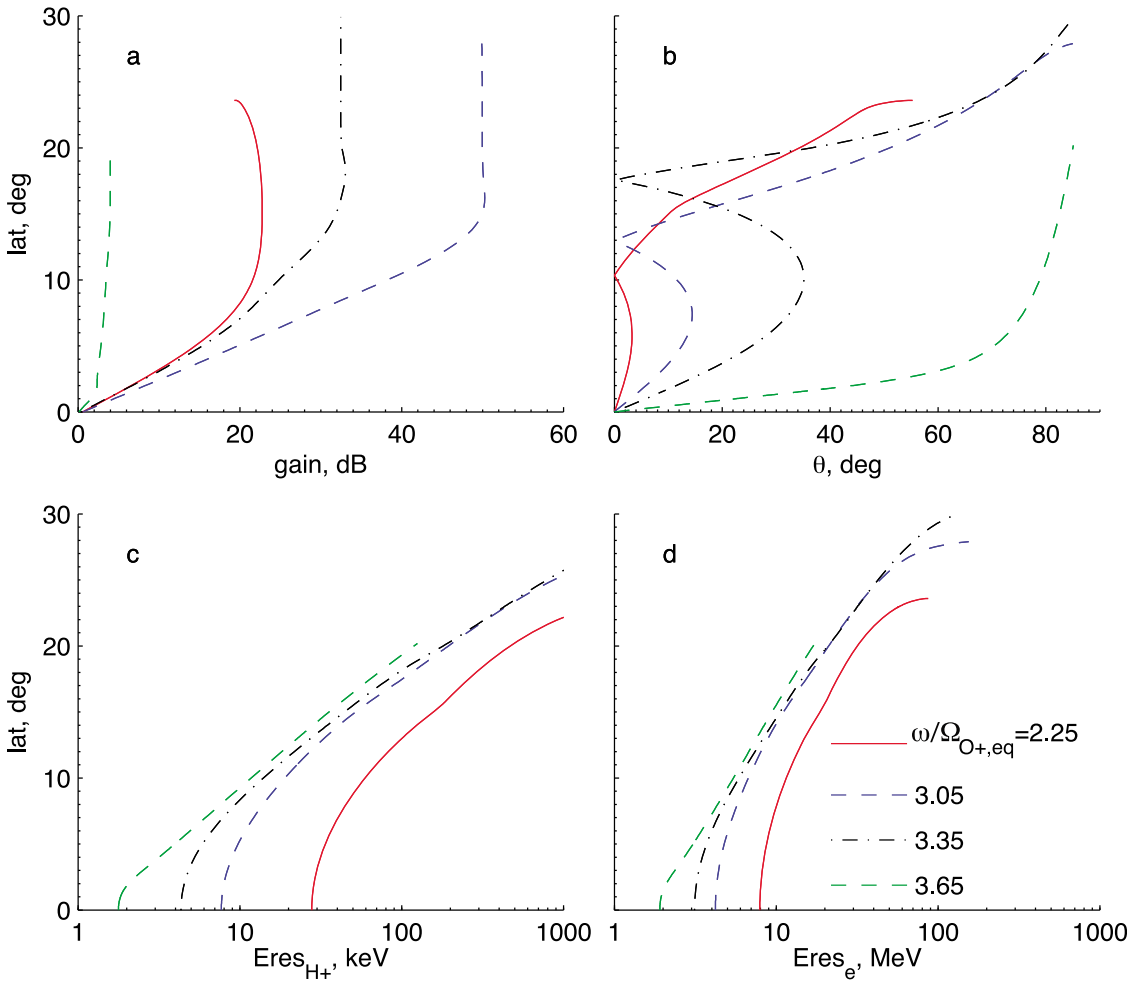

Figure 5. Example of ray tracing for waves launched from the equator at $L = 4.5$, MLT = 19 (which is at the eastward edge of the plasmaspheric plume) during the storm recovery, $t = 48$ h. (a) The path-integrated gain of waves with different normalized wave frequencies, due to ring current H^+ species, as a function of latitude, (b) wave normal angle versus latitude, (c) cyclotron resonant energy of H^+ versus latitude, and (d) cyclotron resonant energy of electron versus latitude.

inately by the charge exchange process. This process also enhances their anisotropy, since those protons with small pitch angle and thus mirroring at low altitudes are preferentially removed. On the westward edge, the decrease in growth rate caused by higher resonant energies (leading to fewer energetic resonant protons) dominates over the increase in growth rate due to the anisotropy enhancement. No significant wave gain occurs on the dayside, even in the region $3 < L < 5$, and $7 <$ MLT < 13 with large $T_\perp/T_\parallel$. This is because of the lower thermal plasma density, which increases the resonant ion energies and reduces the number of resonant protons. There is also no substantial wave gain on the nightside inside the plasmasphere $L \approx 3$, where $T_\perp/T_\parallel - 1$ is large (≈ 2), due to the reduced ring current ion phase space density caused by limited access and strong charge exchange loss at such low L.

[21] At $t = 48$ h, the wave gain is also enhanced inside the plume and the strongest wave gain occurs at the eastward edge of the plume. Furthermore, the wave excitation region extends to just inside the plasmapause on the nightside (second panel in Figure 7) because of three special conditions: the proton anisotropy is enhanced (>1), the total ring current proton density remains high (>6 cm^{-3}), and wave guidance due to the plasmapause density gradient maintains small wave normal angle. The wave gain at $t = 48$ h is generally larger than that at $t = 40$ h, especially at the eastward edge of the plume, due to the increase in proton PSD and anisotropy at this location during the recovery phase (Figures 2d and 3d and Figures 4c and 4d). As the plume narrows, the region of significant gain (>40 dB) also narrows. He^+ band waves with frequency below 2 Ω_{O^+} or above 3.75 Ω_{O^+} cannot be excited (gain less than a few dB) at any location (L, MLT). The lack of low-frequency waves is due to the lower flux of resonant H^+ at the larger resonant velocities, while the lack of high-frequency waves is due to the rapid evolution toward highly oblique wave normal angle, and strong cyclotron damping by the thermal He^+ species at frequencies very close to the He^+ gyrofrequency. Note that the anisotropy and total number density of ring current protons on the dayside is mostly contributed by the low-energy portion of PSD (<5 keV, Figures 4e and 4f), with which only waves with frequency very close to Ω_{He^+} can

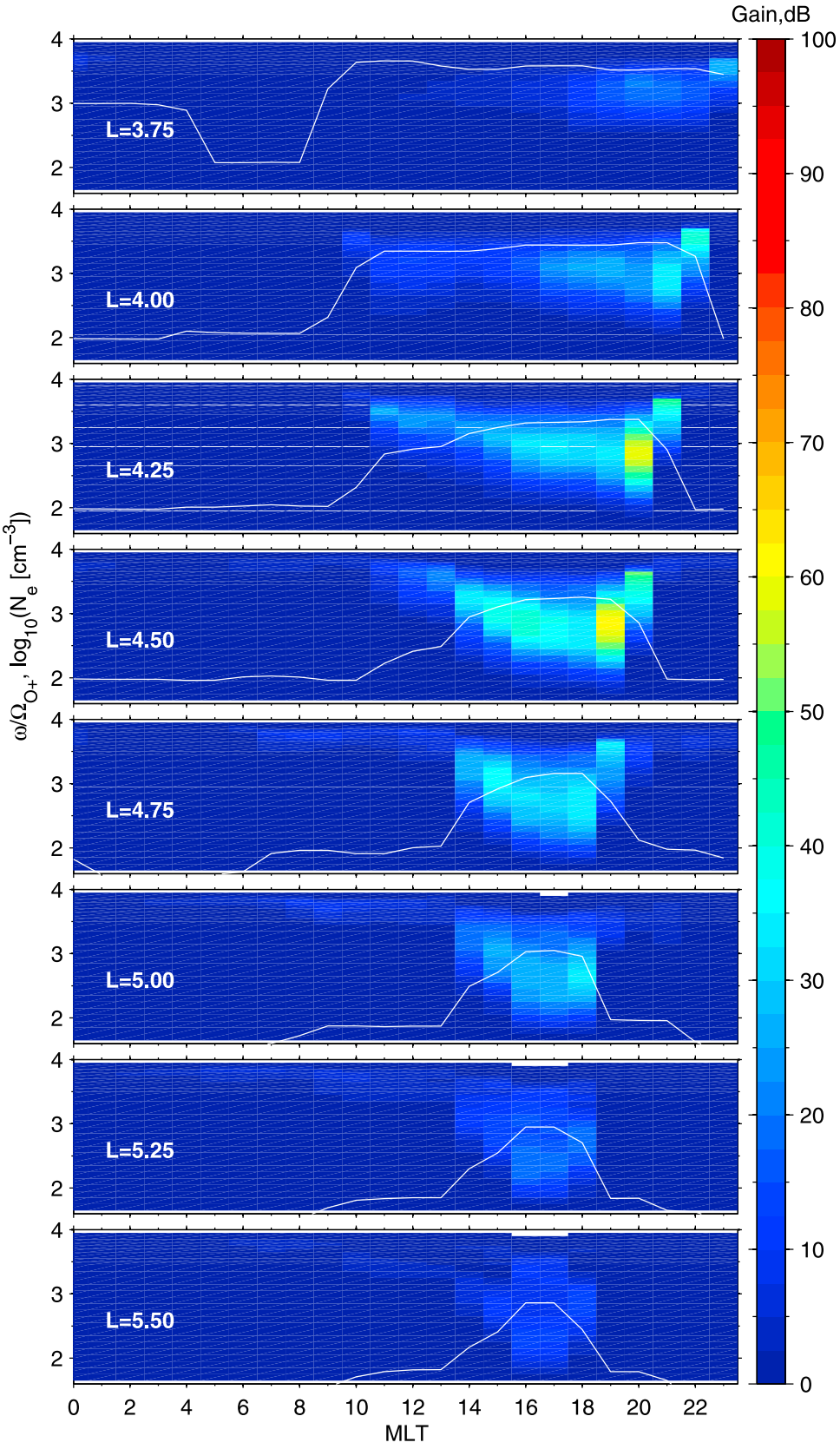

Figure 6. Full gain of EMIC waves in the He^+ band at t = 40 h as a function of wave frequency normalized to the O^+ gyrofrequency and MLT at L from 3.75 to 5.50 every 0.25. The white solid lines denote the quantity $\log_{10}N_e$, where N_e is the equatorial thermal electron density in unit of cm^{-3}, as a function of MLT.

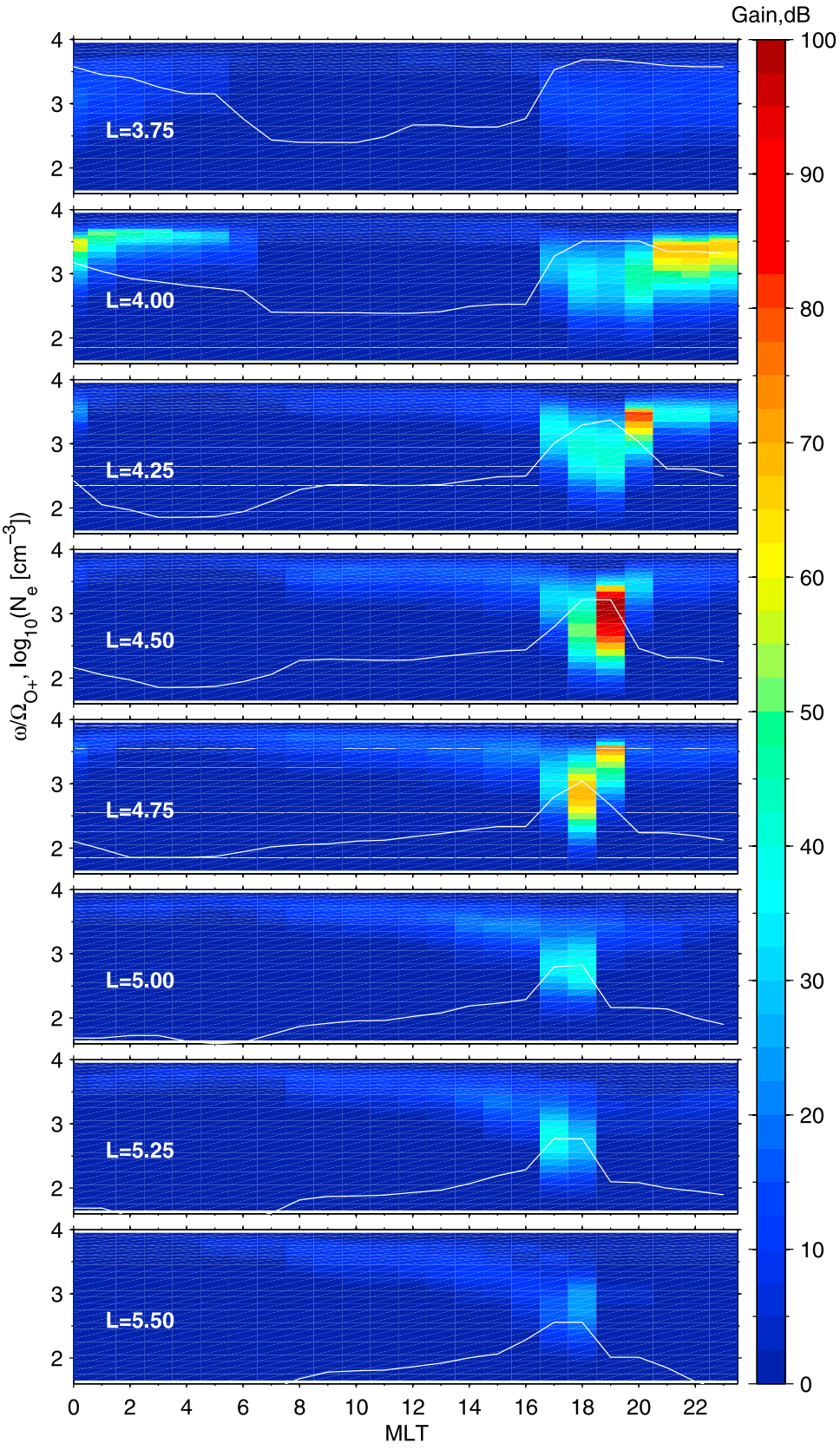

Figure 7. The same as Figure 6 except for t = 48 h.

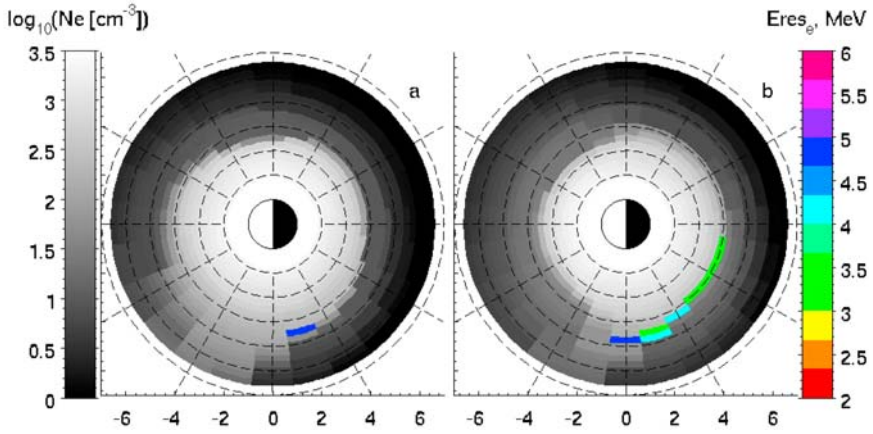

Figure 8. The region of EMIC wave excitation (with equatorial gain >30 dB) in the He^+ band is shown by the colored area for (a) $t = 40$ h and (b) $t = 48$ h. Color coding represents the minimum resonant energy of electron interacting with the excited EMIC waves. The equatorial density is also shown in gray scale on the background.

resonate. However, these waves are inhibited by the two reasons mentioned above. Therefore, no significant wave gain occurs on the dayside during the main phase and even during the recovery phase when the ring current proton density increases and $T_\perp/T_\parallel$ remains high. The ratio of temporal growth rate to the wave frequency γ/ω has been checked and found to be less than 3–4% for all location and at all frequencies of interest, which validates calculation of wave gain obtained from equations (2) and (5).

[22] EMIC waves are also able to resonate with relativistic electrons. To evaluate the minimum electron resonant energy capable of interacting with EMIC waves, we first take the simulated distribution of EMIC wave gain near the equator, which is one half wave gain shown in Figures 6 and 7. 30 dB is chosen as the critical gain, above which the waves are considered to have grown sufficiently to scatter resonant electrons. The region where EMIC wave gain at the equator exceeds this critical gain is shown by the colored area in the Figures 8a and 8b for $t = 40$ and 48 h, respectively. The region of such EMIC waves excitation is confined to the eastward edge of the plume and extends to midnight just inside the plasmapause in the storm recovery. The minimum resonant energy of electrons interacting with excited EMIC waves is also evaluated and color-coded in Figure 8. During the main phase ($t = 40$ h), the minimum resonant energy is above 4.5 MeV, but it is reduced to about 3 MeV during the storm recovery ($t = 48$ h). These scattering events occur preferentially at the eastward edge of the plume and just inside the plasmapause on the nightside.

5. Summary and Discussion

[23] A global model of EMIC wave excitation, based on the RCM, RAM and HOTRAY codes, has been developed and applied to the 21 April 2001 storm. The RCM links solar wind conditions to the injection of plasma sheet particles and supplies the ring current ion energy spectrum at $r = 6.6\ R_E$. The energy spectrum, together with an empirical model for ring current ion composition and anisotropy, is used to derive the MLT and time-dependent boundary condition for the RAM code. The RCM code also provides a self-consistent electric field, which can drive both the convective transport of ring current particles in the inner magnetosphere and the dynamical changes in the plasmaspheric model in the RAM simulation. The RAM code follows the evolution of the ring current ion PSD in energy and pitch angle. During the enhanced convection the injected ring current ions develop a distribution function far from bi-Maxwellian, primarily because of the energy-dependent transport associated with the combined electric field drift and magnetic gradient drift. In agreement with previous RAM studies, the simulated ion PSD is shown to be unstable to EMIC wave excitation, especially in the plume region where the thermal plasma density is high and a ring-type energetic ion distribution develops. A new technique is used to evaluate the global distribution of EMIC waves in the He^+ band in the present study. Ray tracing is performed for EMIC waves in the He^+ band at various locations based on simulated plasmaspheric density from the RAM model, and path-integrated gain is calculated with a combination of ray tracing and evaluation of local temporal growth. The local growth rate is derived from the PSD of ring current ions from RAM simulation using equation (2), which is applicable for arbitrary PSD. This allows us to evaluate the global distribution of EMIC excitation and the spectral properties of these waves. The principal conclusions of this initial simulation are as follows:

[24] 1. EMIC waves in the He^+ band are preferentially excited by the anisotropic ring current H^+ distribution inside the storm time plume, particularly at the eastward edge of the plume, and just inside the plasmapause in the sector from dusk to midnight. The wave gain during the recovery phase is more intense than during the main phase, however, we note that wave-particle interactions were not included in the present RAM simulation. Pitch angle scattering by EMIC waves will reduce the anisotropy of ring current protons and further reduce the wave growth [e.g., *Jordanova et al.*, 2001, 2007].

[25] 2. The wave spectrum inside the plume extends from above 2 Ω_{O^+} to 3.5 Ω_{O^+}. The wave excited at the eastward edge of the plume and just inside the plasmapause can occur at wave frequencies up to 3.7 Ω_{O^+}. The simulated ring current

protons also provide wave growth for EMIC waves with frequencies above >3.7 Ω_{O^+}, but these waves are suppressed at all the locations because such waves quickly become highly oblique and are also strongly damped by cyclotron absorption of thermal He^+.

[26] Excited EMIC waves are able to resonate with electrons as low as 3 MeV at the east edge of the plume and just inside the plasmapause in the premidnight sector during the recovery phase of the April 2001 storm. Minimum electron cyclotron resonant energy during the main phase is found to be above 4.5 MeV at the edge of the plume.

[27] The global distribution of EMIC wave gain presented above is generally consistent with the observations of the MLT distribution of waves obtained from previous observational studies [e.g., *Erlandson and Ukhorskiy*, 2001, *Meredith et al.*, 2003] and with scattering of protons in detached subauroral proton arcs, which has been linked to the location of plumes [*Spasojević et al.*, 2004]. However, there are several improvements, which we plan to incorporate, to make the simulation more realistic in future modeling. The first is to include the effect of quasi-linear relaxation on the evolving ion distributions in the spatial regions where EMIC instability is predicted. The ring-type ion distribution, which develops during transport and loss, should also be unstable to the excitation of equatorial magnetosonic waves [e.g., *Boardsen et al.*, 1992, *Horne et al.*, 2000] and the quasi-linear scattering by such waves will also need to be incorporated into the evolving ion distribution. A recent study [*Chen et al.*, 2009] has shown that wave gain can be enhanced and the minimum resonant electron energy can be reduced by the presence of density fluctuations inside the plume. This structure is not included in the present simulation, but we intend to simulate this in the future by artificially adding electric field fluctuations to the RCM-simulated electric field. Finally, O^+ is an important component of ring current ions, which needs to be included in the evaluation of net wave amplification. Energetic O^+ ions ($\approx$ a few to tens keV) can contribute to damp EMIC waves over all frequencies in the He^+ band [*Kozyra et al.*, 1984, *Jordanova et al.*, 1997]. The effect of damping due to O^+ species should be evaluated, based on improved RAM simulation with a more realistic ion composition at the RAM outer boundary.

[28] The simulation of the global distribution of plasma waves during storm time condition can also be applied for EMIC waves in other frequency range, e.g., in the O^+ band ($\omega < \Omega_{O^+}$) and in the H^+ band ($\Omega_{He^+} < \omega < \Omega_{H^+}$). In a related study, a similar approach has been used to obtain the global distribution of chorus waves, using the ring current electron PSD from RAM simulation [*Jordanova et al.*, 2010]. Understanding the global excitation of these two important magnetospheric emissions, and their variability during storm conditions, is a necessary prerequisite for modeling the global dynamic evolution of radiation belt electrons and ring current ions during storms.

[29] **Acknowledgments.** This research was supported by NASA grants NNX08A135G, NNH08AJ01I, NNG08EK60I, and NNH08AJ01I. The work by C.-P. Wang, M. Gkioulidou, and L. R. Lyons has been supported by NASA grants NNX07AF66G, NNX07AG42G, NNX08A135G, and NNX09AQ41H, and NSF grant ATM-0819864. We thank Richard Wolf at Rice University, who has generously provided us the RCM code, and Robert Spiro at Rice University for helping us get the RCM running at UCLA.

[30] Bob Lysak thanks Nigel Meredith and Colin Waters for their assistance in evaluating this paper.

References

Albert, J. M. (2003), Evaluation of quasi-linear diffusion coefficients for EMIC waves in a multispecies plasma, *J. Geophys. Res.*, *108*(A6), 1249, doi:10.1029/2002JA009792.

Ashour-Abdalla, M., and C. F. Kennel (1978), Nonconvective and convective electron cyclotron harmonic instabilities, *J. Geophys. Res.*, *83*, 1531–1543, doi:10.1029/JA083iA04p01531.

Boardsen, S. A., D. L. Gallagher, D. A. Gurnett, W. K. Peterson, and J. L. Green (1992), Funnel-shaped, low-frequency equatorial waves, *J. Geophys. Res.*, *97*, 14,967, doi:10.1029/92JA00827.

Bräysy, T., K. Mursula, and G. Marklund (1998), Ion cyclotron waves during a great magnetic storm observed by Freja double-probe electric field instrument, *J. Geophys. Res.*, *103*, 4145–4156, doi:10.1029/97JA02820.

Chen, L., R. M. Thorne, and R. B. Horne (2009), Simulation of EMIC wave excitation in a model magnetosphere including structured high-density plumes, *J. Geophys. Res.*, *114*, A07221, doi:10.1029/2009JA014204.

Cornwall, J. M., and M. Schulz (1971), Electromagnetic ion-cyclotron instabilities in multicomponent magnetospheric plasmas, *J. Geophys. Res.*, *76*, 7791–7796, doi:10.1029/JA076i031p07791.

Erlandson, R., and A. Ukhorskiy (2001), Observations of electromagnetic ion cyclotron waves during geomagnetic storms: Wave occurrence and pitch angle scattering, *J. Geophys. Res.*, *106*(A3), 3883–3895.

Gkioulidou, M., C.-P. Wang, L. R. Lyons, and R. A. Wolf (2009), Formation of the Harang reversal and its dependence on plasma sheet conditions: Rice convection model simulations, *J. Geophys. Res.*, *114*, A07204, doi:10.1029/2008JA013955.

Goldstein, J., B. R. Sandel, M. F. Thomsen, M. Spasojević, and P. H. Reiff (2004), Simultaneous remote sensing and in situ observations of plasmaspheric drainage plumes, *J. Geophys. Res.*, *109*, A03202, doi:10.1029/2003JA010281.

Gomberoff, L., and R. Neira (1983), Convective growth rate of ion cyclotron waves in a $H^+ - He^+$ and $H^+ - He^+ - O^+$ plasma, *J. Geophys. Res.*, *88*, 2170–2174.

Horne, R. B. (1989), Path-integrated growth of electrostatic waves: The generation of terrestrial myriametric radiation, *J. Geophys. Res.*, *94*(A7), 8895–8909.

Horne, R. B., and R. Thorne (1993), On the preferred source location for the convective amplification of ion cyclotron waves, *J. Geophys. Res.*, *98*(A6), 9233–9247.

Horne, R. B., and R. Thorne (1994), Convective instabilities of electromagnetic ion cyclotron waves in the outer magnetosphere, *J. Geophys. Res.*, *99*(A9), 17,259–17,273.

Horne, R. B., and R. Thorne (1997), Wave heating of He^+ by electromagnetic ion cyclotron waves in the magnetosphere: Heating near the H^+–He^+ bi-ion resonance frequency, *J. Geophys. Res.*, *102*(A6), 11,457–11,471.

Horne, R. B., G. V. Wheeler, and H. S. C. K. Alleyne (2000), Proton and electron heating by radially propagating fast magnetosonic waves, *J. Geophys. Res.*, *105*, 27,597–27,610, doi:10.1029/2000JA000018.

Jordanova, V. K., L. M. Kistler, J. U. Kozyra, G. V. Khazanov, and A. F. Nagy (1996), Collisional losses of ring current ions, *J. Geophys. Res.*, *101*, 111–126, doi:10.1029/95JA02000.

Jordanova, V. K., J. U. Kozyra, A. F. Nagy, and G. V. Khazanov (1997), Kinetic model of the ring current-atmosphere interactions, *J. Geophys. Res.*, *102*, 14,279–14,292, doi:10.1029/96JA03699.

Jordanova, V. K., C. J. Farrugia, J. M. Quinn, R. B. Torbert, J. E. Borovsky, R. B. Sheldon, and W. K. Peterson (1999), Simulation of off-equatorial ring current ion spectra measured by Polar for a moderate storm at solar minimum, *J. Geophys. Res.*, *104*, 429–436, doi:10.1029/98JA02658.

Jordanova, V. K., C. J. Farrugia, R. M. Thorne, G. V. Khazanov, G. D. Reeves, and M. F. Thomsen (2001), Modeling ring current proton precipitation by electromagnetic ion cyclotron waves during the May 14–16, 1997, storm, *J. Geophys. Res.*, *106*, 7–22, doi:10.1029/2000JA002008.

Jordanova, V. K., Y. S. Miyoshi, S. Zaharia, M. F. Thomsen, G. D. Reeves, D. S. Evans, C. G. Mouikis, and J. F. Fennell (2006), Kinetic simulations of ring current evolution during the Geospace Environment Modeling challenge events, *J. Geophys. Res.*, *111*, A11S10, doi:10.1029/2006JA011644.

Jordanova, V. K., M. Spasojevic, and M. F. Thomsen (2007), Modeling the electromagnetic ion cyclotron wave-induced formation of detached subauroral proton arcs, *J. Geophys. Res.*, *112*, A08209, doi:10.1029/2006JA012215.

Jordanova, V. K., J. Albert, and Y. Miyoshi (2008), Relativistic electron precipitation by EMIC waves from self-consistent global simulations, *J. Geophys. Res.*, *113*, A00A10, doi:10.1029/2008JA013239.

Jordanova, V. K., R. M. Thorne, W. Li, and Y. Miashi (2010), Excitation of whistler-mode chorus from global ring current simulations, *J. Geophys. Res.*, *115*, A00F10, doi:10.1029/2009JA014810.

Kennel, C. (1966), Low-frequency whistler mode, *Phys. Fluids*, *9*, 2190–2202, doi:10.1063/1.1761588.

Kennel, C., and H. Petschek (1966), Limit on stably trapped particle fluxes, *J. Geophys. Res.*, *71*(1), 1–28.

Kozyra, J. U., T. E. Cravens, A. F. Nagy, E. G. Fontheim, and R. S. B. Ong (1984), Effects of energetic heavy ions on electromagnetic ion cyclotron wave generation in the plasmapause region, *J. Geophys. Res.*, *89*, 2217–2233, doi:10.1029/JA089iA04p02217.

Li, W., Y. Y. Shprits, and R. M. Thorne (2007), Dynamic evolution of energetic outer zone electrons due to wave-particle interactions during storms, *J. Geophys. Res.*, *112*, A10220, doi:10.1029/2007JA012368.

Lyons, L. R., and R. M. Thorne (1973), Equilibrium structure of radiation belt electrons, *J. Geophys. Res.*, *78*, 2142–2149, doi:10.1029/JA078i013p02142.

Meredith, N. P., R. M. Thorne, R. B. Horne, D. Summers, B. J. Fraser, and R. R. Anderson (2003), Statistical analysis of relativistic electron energies for cyclotron resonance with EMIC waves observed on CRRES, *J. Geophys. Res.*, *108*(A6), 1250, doi:10.1029/2002JA009700.

Rasmussen, C. E., S. M. Guiter, and S. G. Thomas (1993), A two-dimensional model of the plasmasphere-Refilling time constants, *Planet. Space Sci.*, *41*, 35–43, doi:10.1016/0032-0633(93)90015-T.

Roeder, J. L., M. W. Chen, J. F. Fennell, and R. Friedel (2005), Empirical models of the low-energy plasma in the inner magnetosphere, *Space Weather*, *3*, S12B06, doi:10.1029/2005SW000161.

Shprits, Y. Y., L. Chen, and R. M. Thorne (2009), Simulations of pitch angle scattering of relativistic electrons with MLT-dependent diffusion coefficients, *J. Geophys. Res.*, *114*, A03219, doi:10.1029/2008JA013695.

Spasojević, M., J. Goldstein, D. L. Carpenter, U. S. Inan, B. R. Sandel, M. B. Moldwin, and B. W. Reinisch (2003), Global response of the plasmasphere to a geomagnetic disturbance, *J. Geophys. Res.*, *108*(A9), 1340, doi:10.1029/2003JA009987.

Spasojević, M., H. U. Frey, M. F. Thomsen, S. A. Fuselier, S. P. Gary, B. R. Sandel, and U. S. Inan (2004), The link between a detached subauroral proton arc and a plasmaspheric plume, *Geophys. Res. Lett.*, *31*, L04803, doi:10.1029/2003GL018389.

Summers, D., and R. M. Thorne (1991), The modified plasma dispersion function, *Phys. Fluids B*, *3*, 1835–1847, doi:10.1063/1.859653.

Summers, D., and R. M. Thorne (2003), Relativistic electron pitch-angle scattering by electromagnetic ion cyclotron waves during geomagnetic storms, *J. Geophys. Res.*, *108*(A4), 1143, doi:10.1029/2002JA009489.

Thorne, R. M., and R. B. Horne (1992), The contribution of ion-cyclotron waves to electron heating and SAR-arc excitation near the storm time plasmapause, *Geophys. Res. Lett.*, *19*, 417–420, doi:10.1029/92GL00089.

Thorne, R. M., and R. B. Horne (1994), Energy transfer between energetic ring current $H^+$and O^+ by electromagnetic ion cyclotron waves, *J. Geophys. Res.*, *99*, 17,275, doi:10.1029/94JA01007.

Thorne, R. M., and R. B. Horne (1997), Modulation of electromagnetic ion cyclotron instability due to interaction with ring current O^+ during magnetic storms, *J. Geophys. Res.*, *102*(A7), 14,155–14,163.

Thorne, R. M., and C. F. Kennel (1971), Relativistic electron precipitation during magnetic storm main phase, *J. Geophys. Res.*, *76*(19), 4446–4453.

Thorne, R. M., R. B. Horne, V. K. Jordanova, J. Bortnik, and S. Glauert (2006), Interaction of EMIC waves with thermal plasma and radiation belt particles, in *Magnetospheric ULF Waves: Synthesis and New Directions*, *Geophys. Monogr. Ser.*, vol. 169, edited by K. Takahashi et al., p. 213, AGU, Washington, D. C.

Toffoletto, F., S. Sazykin, R. Spiro, and R. Wolf (2003), Inner magnetospheric modeling with the Rice Convection Model, *Space Sci. Rev.*, *107*, 175–196, doi:10.1023/A:1025532008047.

Tsyganenko, N. A. (1995), Modeling the Earth's magnetospheric magnetic field confined within a realistic magnetopause, *J. Geophys. Res.*, *100*, 5599–5612, doi:10.1029/94JA03193.

Tsyganenko, N. A. (1996), Effects of the solar wind conditions in the global magnetospheric configurations as deduced from data-based field models (invited), in *Proceedings of International Conference on Substorms*, *ESA Spec. Publ.*, vol. 389, edited by E. J. Rolfe and B. Kaldeich, p. 181, Eur. Space Agency, Paris.

Wang, C.-P., L. R. Lyons, T. Nagai, J. M. Weygand, and R. W. McEntire (2007), Sources, transport, and distributions of plasma sheet ions and electrons and dependences on interplanetary parameters under northward interplanetary magnetic field, *J. Geophys. Res.*, *112*, A10224, doi:10.1029/2007JA012522.

Xiao, F., Q. Zhou, H. He, H. Zheng, and S. Wang (2007), Electromagnetic ion cyclotron waves instability threshold condition of suprathermal protons by kappa distribution, *J. Geophys. Res.*, *112*, A07219, doi:10.1029/2006JA012050.

Young, D. T., S. Perraut, A. Roux, C. de Villedary, R. Gendrin, A. Korth, G. Kremser, and D. Jones (1981), Wave-particle interactions near Ω_{He^+} observed on GEOS 1 and 2: 1. Propagation of ion cyclotron waves in He^+-rich plasma, *J. Geophys. Res.*, *86*, 6755–6772, doi:10.1029/JA086iA08p06755.

Young, D. T., H. Balsiger, and J. Geiss (1982), Correlations of magnetospheric ion composition with geomagnetic and solar activity, *J. Geophys. Res.*, *87*, 9077–9096, doi:10.1029/JA087iA11p09077.

L. Chen, M. Gkioulidou, L. Lyons, R. M. Thorne, and C.-P. Wang, Department of Atmospheric Sciences, University of California, Los Angeles, CA 90024, USA. (clj@atmos.ucla.edu)

R. B. Horne, British Antarctic Survey, Natural Environment Research Council, Cambridge CB3 0ET, UK.

V. K. Jordanova, Los Alamos National Laboratory, Los Alamos, NM 87545, USA.